

THE STRUCTURE OF THE STRONGLY LENSED GAMMA-RAY SOURCE B2 0218+35

ANNA BARNACKA^{1,2}, MARGARET J. GELLER¹, IAN P. DELL'ANTONIO³, AND ADI ZITRIN⁴

¹Harvard-Smithsonian Center for Astrophysics, 60 Garden St, MS-20, Cambridge, MA 02138, USA

²Astronomical Observatory, Jagiellonian University, Cracow, Poland

³Department of Physics, Brown University, Box 1843, Providence, RI 02912

⁴Cahill Center for Astronomy and Astrophysics, California Institute of Technology, MC 249-17, Pasadena, CA 91125, USA

Draft version July 24, 2022

ABSTRACT

Strong gravitational lensing is a powerful tool for resolving the high energy universe. We combine the temporal resolution of *Fermi*-LAT, the angular resolution of radio telescopes, and the independently and precisely known Hubble constant from *Planck*, to resolve the spatial origin of gamma-ray flares in the strongly lensed source B2 0218+35. The lensing model achieves 1 milliarcsecond spatial resolution of the source at gamma-ray energies. The data imply that the gamma-ray flaring sites are separate from the radio core: the bright gamma-ray flare (MJD: 56160 - 56280) occurred 51 ± 8 pc from the 15 GHz radio core, toward the central engine. This displacement is significant at the $\sim 3\sigma$ level, and is limited primarily by the precision of the Hubble constant. B2 0218+35 is the first source where the position of the gamma-ray emitting region relative to the radio core can be resolved. We discuss the potential of an ensemble of strongly lensed high energy sources for elucidating the physics of distant variable sources based on data from *Chandra* and SKA.

Subject headings: Galaxies: active – gravitational lensing: strong –gamma-rays: jets

1. INTRODUCTION

The high-energy universe is dominated by extreme and violently variable objects. The powerful jets of relativistic plasma associated with these sources are the largest and the most efficient particle accelerators known. The energy source, the energy dissipation mechanism and the particle acceleration mechanism in these fast flares of non-thermal radiation remain puzzling. Proposed mechanisms include relativistic shocks and magnetic reconnection (Zenitani & Hoshino 2001; Stawarz & Ostrowski 2002; Lyutikov & Uzdensky 2003; Kirk & Skjæraasen 2003; Jaroschek et al. 2004; Lyubarsky 2005; Proga 2005; McKinney 2006; Zenitani & Hoshino 2007; Komissarov et al. 2007; Zweibel & Yamada 2009; Giannios et al. 2009; Tchekhovskoy et al. 2010; Nalewajko et al. 2011; Tchekhovskoy et al. 2011; Cerutti et al. 2012; Hoshino 2012; Sironi & Spitkovsky 2014; Nalewajko et al. 2015; Moscibrodzka et al. 2015; Broderick & Tchekhovskoy 2015; MacDonald et al. 2015).

One of the limitations to understanding these sources is the inability to localize the spatial origin of the emission. This failure is a direct result of the poor resolution of gamma-ray telescopes that reach, at best, an angular resolution of 0.1 deg. This angular resolution is unlikely to improve substantially with future instruments because it is limited by fundamental physical effects including nuclear recoil.

Gravitational lensing magnifies distant sources. Thus lensed gamma-ray blazars offer the best opportunity for resolving the locations of the emitting regions. For example, the bright blazar PKS 1830-211 is a lensed system (Barnacka et al. 2011). Analysis of the time delays during flaring episodes, combined with the lens model for this source reveals that two gamma-ray flares originated from a region within 100 pc from the central engine. Two ad-

ditional gamma-ray flares originated at least 1.5 kpc from the central engine (Barnacka et al. 2015a). These multiple variable emitting regions along the jet pose challenges for understanding the particle acceleration mechanism.

A second gravitationally lensed blazar B2 0218+35 offers further opportunities to explore the origin of the variable gamma-ray emission. This well-observed system has a number of features that enable the derivation of strong constraints on the nature of the gamma-ray source. The lens galaxy, observed with HST, is surprisingly simple and isolated (Wucknitz et al. 2004). There are extensive high-resolution radio observations of the lensed radio jet at several wavelengths. The *Fermi*-LAT light curve includes two flares, one of long duration and one short flare.

Based on the optical observations of the lens system and the radio observations of the lensed source, we demonstrate that the positions of the radio core and jet can be localized to 1 milliarcsecond. Localization of the gamma-ray source relative to the radio emitting regions requires both the time resolution of the *Fermi*-LAT light curve and a well-measured Hubble constant (Barnacka et al. 2014a, 2015b).

The *Fermi*-LAT light curves provide time delays with an accuracy of a few hours. If the time delay originates from the resolved radio core, the associated Hubble constant should be the true value obtained with independent techniques. If there is an offset of even a few milliarcseconds between the gamma-ray emitting region and the radio core, the time delay will imply a Hubble constant that differs from the true value measured with many independent methods (Freedman et al. 2001; Freedman & Madore 2010; Suyu et al. 2010; Riess et al. 2011a,b; Freedman et al. 2012; Chávez et al. 2012; Efstathiou 2014; Suyu et al. 2013). Evidently, if the Hubble constant is well-known, the offset between the gamma-ray emitting region and the radio core can be derived

with remarkable significance limited only by the accuracy of the time delay and the independently determined Hubble constant (Barnacka et al. 2015b).

We introduce the optical and radio observations of the gravitationally lensed blazar B2 0218+35 and we reconstruct the properties of the lens and the source (Sections 2 and 3). In Section 4, we use the Fermi-LAT data to explore the gamma-ray properties of B2 0218+35. We focus on two gamma-ray flares where we measure gravitationally induced time delays (Section 5). In Section 6, we combine the measurements of the gamma-ray time delays, the well-resolved position of the radio core, the reconstructed gravitational potential of the lens, and we explore the relative spatial origin of the two gamma-ray flares. Finally, we apply the Hubble parameter tuning approach, where we use the independently measured Hubble constant to localize the gamma ray emission relative to the radio core. We compare the results for B2 0218+35 with those for PKS 1830-211. We discuss the implications of the source structure for gamma-ray emission mechanisms in Section 7. We also propose extension of this approach to sources that will be observed with SKA and *Chandra*. We conclude in Section 8.

2. B2 0218+35: A GRAVITATIONALLY-LENSED SYSTEM

B2 0218+35 is a gravitationally-lensed system with the smallest known Einstein radius (330 mas) (O’Dea et al. 1992; Patnaik et al. 1995). The system consists of a bright blazar at redshift $z_S = 0.944 \pm 0.002$ (Cohen et al. 2003), lensed by an apparently isolated spiral galaxy at redshift $z = 0.6847$ (Browne et al. 1993). The lens bends the emission of the jet into two bright images of the core and extended structures, including an Einstein ring (Patnaik et al. 1992; O’Dea et al. 1992; Patnaik et al. 1993, 1995; Jackson et al. 2000; Biggs et al. 2001, 2003).

The well-resolved radio images show clear jet-like structures. Wucknitz et al. (2004) shows that the jet sub-components are located exactly radially with respect to the center of mass of the lens. The existence of the radio ring implies radial alignment of the jet on scales \lesssim kpc.

The first measurement of the time delay using VLA 15 GHz polarization observations yielded a value of 12 ± 3 days (Corbett et al. 1996). Biggs et al. (1999) used the results of a three-month VLA monitoring campaign at two frequencies and obtained a time delay of 10.5 ± 0.4 days. Cohen et al. (2000) used high-precision VLA flux density measurements, over the same epoch as Biggs et al. (1999), and measured a time delay of $10.1^{+1.5}_{-1.6}$ days.

This system has been a “golden lens” for Hubble constant measurement (Wucknitz et al. 2004). However, despite precise measurements of the time delay, a clean lens environment without nearby companions or a surrounding cluster, and a negligible number of structures along the line of sight which would complicate the modeling of the lens, the H_0 values derived from this system are in the range $61\text{--}78 \text{ km s}^{-1} \text{ Mpc}^{-1}$ (York et al. 2005; Lehár et al. 2000; Wucknitz et al. 2004). The most recent attempt to measure H_0 for B2 0218+35, using a time delay of 11.46 ± 0.16 days based on gamma-ray emission, results in a Hubble constant of $64 \pm 4 \text{ km s}^{-1} \text{ Mpc}^{-1}$ (Cheung et al. 2014).

This large scatter in the H_0 values can indicate complex source structure (Barnacka et al. 2015b). To investigate

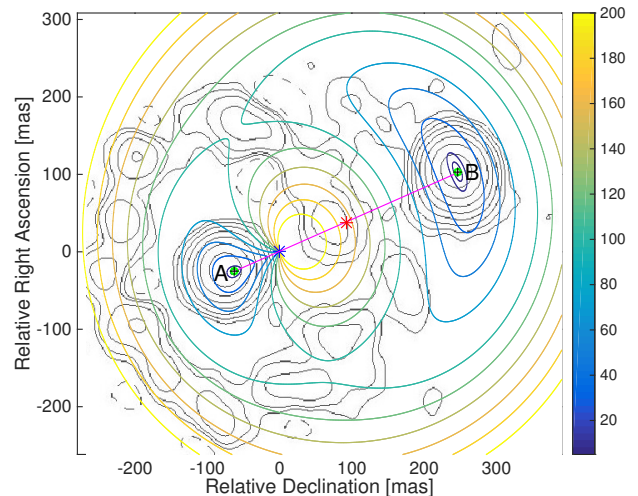


FIG. 1.— Image plane. The colored contours show the Fermat potential. The coordinates are relative to the reconstructed lens position. Black crosses show the reconstructed mirage image positions. Green open circles show the positions of the 15 GHz mirage images of B2 0218+35. The gray contours show the radio emission observed at 1.687 GHz. The magenta line indicates the axis connecting the mirage images. The blue star shows the final position of the lens center. The red star indicates the reconstructed position of the 15 GHz radio source.

the detailed source structure, we build a lens model.

3. B2 0218+35 AS A HIGH RESOLUTION COSMIC TELESCOPE

B2 0218+35 is a perfect system for lens modeling. The simplicity and isolation of the lensing galaxy results in a clean gravitational lens potential. Previous lens models show that the observations are consistent with a Singular Isothermal Sphere (SIS) model for the mass distribution of the lens (Wucknitz et al. 2004; Larchenkova et al. 2011). These studies focused on the properties of the lensing galaxy and measurement of the Hubble parameter (York et al. 2005). Here, we use the lens as a high-resolution telescope to investigate the structure of the source over wavelengths ranging from radio to gamma-ray energies. We first use the lens model to determine an accurate position for the radio core. We evaluate the uncertainties in the model using Monte Carlo simulations.

3.1. Constraining the Lens

We base the model on radio VLBA observations at 15 GHz, where the position of mirage images of the core are measured with 0.6 mas accuracy (1994 Oct 3, Patnaik et al. 1995). The position of the mirage image B (brighter image located outside the Einstein ring; green circle in Figure 1) with respect to image A (green circle, Figure 1), along with all the parameters, are summarized in Table 1.

The positions of the 15 GHz mirage images yield a measure of the Einstein radius and the position of the source. The Einstein radius of the lens, with a mass distribution close to a SIS, is half the distance between the mirage images; $\theta_E = (\theta_A + \theta_B)/2 = 167.2 \pm 0.6$ mas. The corresponding lens mass within one Einstein radius is $\sim 2 \times 10^{10} M_\odot$. For a lens of such a small mass, resolution of the mirage images is possible only with high-resolution imaging.

TABLE 1
INPUT PARAMETERS FOR THE LENS MODELING

Parameter	Value
Image A at 15 GHz	(0,0)
Image B at 15 GHz	$(309.2, -127.4) \pm 0.6$ mas ^a
Estimated Source Position	$(154.6, -63.7) \pm 10$ mas
Einstein Angle	$\theta_E = 167.2 \pm 0.6$ mas
Approximate Lens Position	$(56, -23) \pm 20$ mas
Optical Center of the Galaxy ^b	
– no masking	$(57 \pm 4, 1 \pm 6)$
– spiral arms masked	$(75 \pm 6, -6 \pm 13)$
Position Angle	$\phi_0 = 49^\circ$ ^c
Time Delay at 15 GHz	10.1 ± 1.6 days ^d , 10.5 ± 0.4 days ^e
Magnification Ratio at 15 GHz	3.623 ± 0.065 ^f
Source Redshift	$z_S = 0.944$ ^g ,
Lens (Galaxy) Redshift	$z_L = 0.6847$ ^h

^aPatnaik et al. (1995)

^bYork et al. (2005)

^cYork et al. (2005)

^dCohen et al. (2000)

^eBiggs et al. (1999)

^fPatnaik et al. (1995)

^gCohen et al. (2003)

^hBrowne et al. (1993)

The mirage images appear on the axis defined by the position of the source and the lens (magenta line in Figure 1), at distances of $\pm\theta_E$ from the source. The source is located at half the distance between the mirage images, $\theta_S = (\theta_A - \theta_B)/2$. The source position may deviate from the axis if the mass distribution deviates from a SIS. In the model described below, we thus search for the best source position within 10 mas from this estimate.

The last, major unknown is the position of the lens. York et al. (2005) derived the optical center of the galaxy with an accuracy of ~ 15 mas (see Table 1). We seek a center of mass reconstructed to ~ 1 mas. We first take the position of the lens as inferred from the optical images. Then, as an additional constraint, we use the lens geometry; the lens must be located close to the image axes and to the center of the Einstein ring (Figure 1).

For demonstration purposes, in Figure 1 we display the contours of radio emission observed at 1.687 GHz with a beam FWHM of 50×50 mas. However, this image was available to us only in jpg format downloaded from JVAS ¹. We rescaled it by $\sim 5\%$ to align it with well-resolved mirage images at 15 GHz. The image at 1.687 GHz resolves the mirage images of the core and the Einstein ring structures. After rescaling, the center of the ring indicates a plausible position of the lens with an accuracy of ~ 50 mas. Using all of this information, we find the approximate position of the lens (see Table 1). In the lens model described below, we use Monte Carlo simulations to refine the best lens position within this region.

The VLBA observations at 15 GHz also provide a very precise flux density ratio between mirage images of 3.623 ± 0.065 . However, observations of B2 0218+35 at different frequencies and epochs show a large spread in measured magnification ratios, from 1 to 6 (Biggs et al. 1999; Cohen et al. 2000; Cheung et al. 2014). This large spread in magnification ratio may result from different

propagation effects (Mittal et al. 2007), substructures in the mass distribution (Mao & Schneider 1998; Kochanek & Dalal 2004; Metcalf & Amara 2012; Biggs et al. 2004), or even from microlensing (Vovk & Neronov 2015). To avoid this additional complexity, we do not use the flux ratio as a constraint. However the model we construct is consistent with the range.

3.2. Lens Modeling

We investigate the properties of the lens system with a MATLAB code inspired by Zitrin et al. (2009, 2013). We construct a 800×800 mas grid with a resolution of 1 mas. We define coordinates relative to the position of the lens center. We perform all calculations in the image plane because the observed positions of the images are directly linked to the image plane, not to the source plane.

We compute the Fermat surface using Eq. (61) from Narayan & Bartelmann (1996):

$$(\vec{\theta} - \vec{\beta}) - \vec{\nabla}_{\theta}\psi = 0, \quad (1)$$

where $\vec{\theta}$ is the position of a mirage image, $\vec{\beta}$ is the source position, and ψ is the gravitational potential of the lens. The Fermat principle implies that the images form at the extrema (maxima, minima, and saddle points) of the surface (Blandford & Narayan 1986). We then search for the extrema of the Fermat surface using Matlab procedure `extrima2`². Figure 2 shows color contours of the Fermat surface with two minima where the mirage images form. We find the positions of these minima and calculate the offset between their coordinates and positions of the mirage images resolved at 15 GHz.

The position of the images and the gravitational potential of the lens allow us to calculate the time delay between the mirage images. We use Eq (63) from Narayan & Bartelmann (1996):

$$t(\vec{\theta}) = D \frac{(1+z_L)}{c} \left[\frac{1}{2}(\vec{\theta} - \vec{\beta})^2 - \psi(\vec{\theta}) \right], \quad (2)$$

to calculate the time delay between the arrival of photons from image θ_A and θ_B . We then calculate the difference between the estimated time delay and the time delay measured at 15 GHz.

We calculate magnifications of the mirage images using Eqs (55-60) from Blandford & Narayan (1986). This calculation is also based on the gravitational potential and the positions of the mirage image. We do not, however, use the magnification ratio to extract the lens parameters. We provide the formalism because we do use the magnification later to constrain the origin of the gamma-ray radiation.

We seek the gravitational potential along with source and lens locations that produce reconstructed positions of the lensed images and associated time delay in agreement with the 15 GHz observations. To find this solution, we repeat our calculations of the image positions and the time delay between them for a range of parameters. We vary the lens position around the value listed in Table 1. We explore a region of 20 mas with a 1 mas step. We search for the best source position around the value listed in Table 1.

¹ <http://www.jb.man.ac.uk/research/gravlens/lensarch/B0218+357/B0218+357.html>

² <http://www.mathworks.com/matlabcentral/fileexchange/12275-extrema-m-extrema2-m>

We investigated a range of complex models for the gravitational potential. We added parameters including a core, a variable slope for the mass distribution, and a variable ellipticity and position angle of the lensing galaxy. We achieved the best reconstruction for an elliptical singular isothermal sphere (Kneib 2014):

$$\psi(r, \theta) = r\theta_E \sqrt{1 - \epsilon \cos(2(\phi - \phi_0))}, \quad (3)$$

where ϵ is an ellipticity of the gravitational potential, ϕ_0 is the position angle of the potential, and θ_E is an Einstein angle defined as:

$$\theta_E = 4\pi \frac{\sigma_0^2}{c^2} \frac{D_{LS}}{D_{OS}}, \quad (4)$$

where σ_0 is the central velocity dispersion of the 3D velocity field, and D_{LS} and D_{OS} are cosmological distances from the lens to the source, and from the observer to the source, respectively. We also define:

$$D \equiv \frac{D_{OL}D_{OS}}{D_{LS}} = hd, \quad (5)$$

where D_{OL} is the distance from the observer to the lens. The parameter h refers to the Hubble constant, $H_0 = h \times 100 \text{ km s}^{-1} \text{ Mpc}^{-1}$. We calculate distances based on a homogenous Friedmann-Lemaître-Robertson-Walker cosmology, using $h = 0.673$, the mean mass density $\Omega_M = 0.315$ and the normalized cosmological constant $\Omega_\Lambda = 0.686$ (Planck Collaboration et al. 2014).

We define the best reconstructed model as the one which reproduces the positions of the mirage images with the smallest offset, and where the time delay is within 1σ of the measured delay at 15 GHz.

To estimate statistical errors, we use Monte Carlo chain simulations. We based our algorithm on the MCMC toolbox for MatLab³ (Haario et al. 2006).

We test for systematics in our simulations by comparing the numerical solution with an analytic model. The simplest analytic solution is the SIS. We compare the positions of the images, time delays and magnification ratios for the SIS calculated analytically and numerically for positions of the sources across the entire lens plane. The numerical procedure applied on a grid with a 1 mas resolution, on average reconstructs image positions with $\sim 0.3 \text{ mas}$. On average, the time delay is reproduced within 0.01 days, and the magnification ratio within 0.05. This level of precision shows that on a scale of 1 mas, our lens parameters are unaffected by systematic numerical errors.

3.2.1. Lens Modeling Results

Table 1 summarizes the input parameters for the lens model; the ellipticity of the lens, and the source and lens positions. Table 2 shows the model results along with the statistical errors from the Monte Carlo chain simulations.

The fit yields an $\epsilon \sim 0$, essentially an isotropic SIS. We reconstruct the lens and source positions with an accuracy of 1 mas corresponding to 8 pc in the source plane.

The time delay is most sensitive to the distance of the source from the center of the lens. In the radial direction the time delay changes by 0.13 days (3.12 hours) per

TABLE 2
RESULTS OF THE FIT

Parameter	Value
Ellipticity ϵ	0.0057 ± 0.0042
Source Position (x_S, y_S)	$(154.2 \pm 0.8, -62.9 \pm 0.7) \text{ mas}$
Lens Position (x_L, y_L)	$(62.2 \pm 0.9, -25.0 \pm 0.8) \text{ mas}$

TABLE 3
RECONSTRUCTION

Parameter	Value	Difference
Image A	$(-0.4, 0)$	0.4 mas
Image B	$(308.6, -128.0)$	0.85 mas
Time Delay	10.7 days	$\sim 0.2 \text{ days}$
Magnification Ratio	3.85	0.23

1 mas but in the tangential direction it changes much more slowly, 0.01 day per 1 mas.

The lens model predicts the time delay and corresponding magnification ratio along the jet. Figure 2 shows the result. The radial alignment of the jet produces maximal differences in time delay among regions distributed along the jet.

The positions of the mirage images are most sensitive to changes of the source position in the tangential direction relative to the images-lens axis. Changing the source position by 1 mas in the tangential direction, moves the mirage images by 5.5 mas. In the radial direction a 1 mas change in the source position displaces the image by only 2.7 mas. Table 3 and Figure 1 show that the model reproduces the observed mirage image positions to 0.4 – 0.8 mas.

4. B2 0218+35 AS A GAMMA-RAY SOURCE

B2 0218+35 is a bright gamma-ray source. Here, we analyze the gamma-ray light curve observed with the Large Area Telescope onboard the *Fermi* mission (*Fermi*-LAT, Atwood et al. 2009).

We analyze the *Fermi*-LAT P7REP events and spacecraft data of B2 0218+35 during the period MJD: 54682–57041. We use the standard likelihood tools distributed with the Science Tools v9r32p5 package available on the *Fermi* Science Support Center webpage.

We only used events in the CLEAN dataset with the highest probability of being photons. We exclude events with zenith angles $> 100^\circ$ to limit contamination by Earth albedo gamma rays produced by cosmic rays interacting with the upper atmosphere. We also remove events with rocking angles $> 52^\circ$ to eliminate time intervals when the Earth entered the LAT Field of View (FoV).

The selected events with reconstructed energies above 100 MeV within a square region of 10° radius are centered on the coordinates of B2 0218+35 (see Figure 3). We analyze the selected photons with a binned maximum likelihood method (Mattox et al. 1996).

We model the background emission using a galactic diffuse emission model (gll_iem.v05) with an isotropic component (iso_clean.v05; available on the *Fermi* Science Support Center webpage). The fluxes are based on the post-launch instrument response function P7REP_CLEAN_V15.

³ <http://helios.fmi.fi/~lainema/mcmc/>

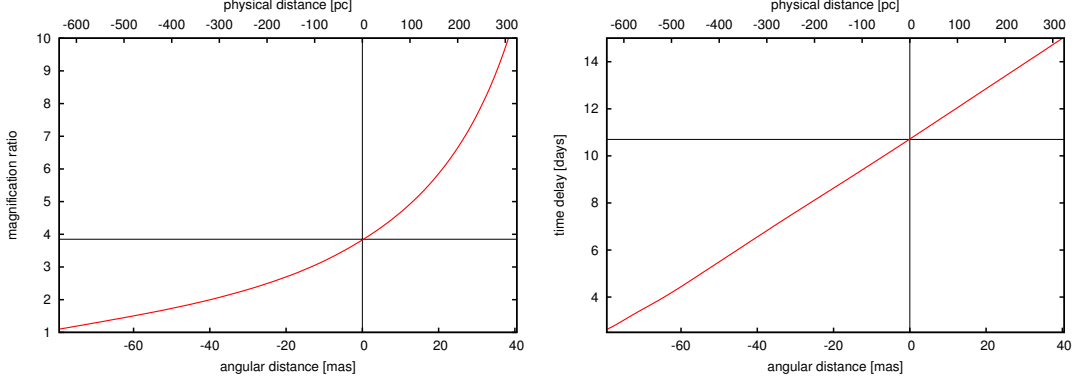


FIG. 2.— Magnification ratios (**Left**) and time delays (**Right**) as a function of the distance between the core and emitting regions along the jet. **Left**: The gray lines indicate the magnification ratio, 3.85, expected at the position of the 15 GHz core. **Right**: The gray lines indicate the time delay of 10.7 days expected for an emitting region coincident with the position of the 15 GHz core.

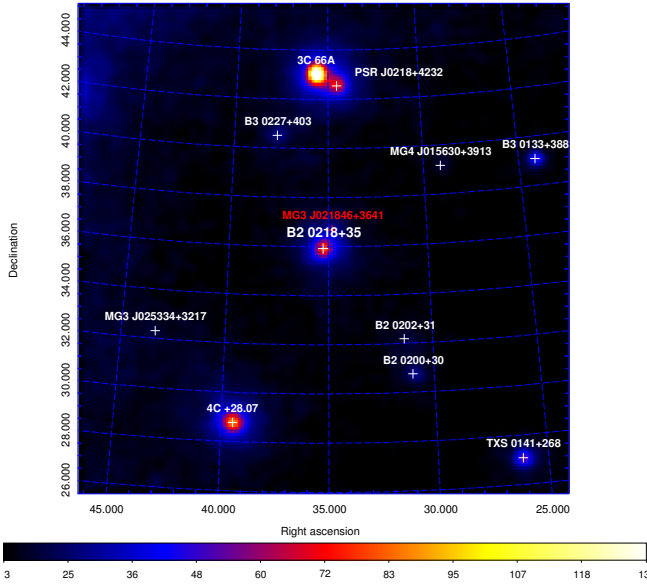


FIG. 3.— *Fermi*-LAT count map of B2 0218+35. The energy range is 100 MeV to 300 GeV.

The XML source model contains all of the sources included in the Second *Fermi*/LAT catalog (Nolan et al. 2012) within an annulus of 20° around B2 0218+35. We first analyze the XML source model fitting the sources within 10° ; within an annulus from 10° to 20° we fix the sources to their 2FGL values. We calculate the test statistic (TS) for all the sources located within the 10° radius during the time period MJD: 54682–57041. Sources with a TS lower than 6.5, corresponding to a statistical significance of $\approx 2.5\sigma$, are then fixed in further analysis. The resulting XML source model is then the basis for the 6.5 year light curve in Figure 4. The TS is also based on this source model.

The TS of B2 0218+35 for this dataset is 8890, corresponding to a statistical significance of $\approx 94\sigma$. The energy spectrum is best described by a power law with $\Gamma = 2.28 \pm 0.02$ and an integral flux of $F(0.1 - 300 \text{ GeV}) = (1.42 \pm 0.05) \times 10^{-7} \text{ ph cm}^{-2} \text{ s}^{-1}$. The highest energy event recorded by *Fermi*/LAT corresponds to $\sim 95.7 \text{ GeV}$. The flux in each time bin is reconstructed in

the same manner as for the full time range; the photon index and integral flux in these bands are free parameters.

Our goal is to investigate the spatial origin of gamma-ray flares. Thus, we look for periods of flaring activity in the gamma-ray light curve of B2 0218+35. We define a flare as a period of time when the emission in a one-day bin increases by at least two sigma relative to the average flux. Note that Figure 4 shows data in 7-day bins.

Based on our definition, we identify two active periods; a very long flare between MJD: 56160 – 56280, and a short flare consisting of a single bright event, occurring between MJD: 56800 – 57000. Figure 5 shows both flares. Visually it may seem that there are other flares in Figure 4. However, these apparent flares are not significant with one-day bins. We use the light curves for the two significant flares to compute time delays.

5. TIME DELAY MEASUREMENT

In the B2 0218+35 system, radio observations reveal two images separated by $\sim 330 \text{ mas}$. The angular resolution of the *Fermi*-LAT detector is $\sim 1^\circ$. Thus the observed gamma-ray light curve is a sum of two unresolved mirage images shifted in time, but with a constant magnification ratio. The temporal resolution of the *Fermi*-LAT detector allows determination of the time delay at gamma ray energies. With sufficiently well-determined time delays, the relationship between the radio and gamma-ray time delays constrain the relative source positions.

The *Fermi*-LAT data cover a long, uninterrupted periods containing the two significant flares. There are several methods for extracting the time delay from these binned data (Barnacka et al. 2015a). We use the standard Autocorrelation Function (ACF), and the more sensitive Double Power Spectrum (DPS) method (Barnacka et al. 2011; Barnacka 2013). The detailed description of the DPS method together with comparison to other methods is described in Barnacka et al. (Section 3.2.2 and Appendix A, 2015a). The DPS is similar to the Cepstrum method (Bogert et al. 1963), where a time series with a delay transforms into Fourier space with the extra component $e^{-2\pi i f a}$, where f is frequency and a is the delay. Squaring the absolute value of this extra component results in a periodic pattern imprinted on the power spectrum. The period of this pattern in the frequency

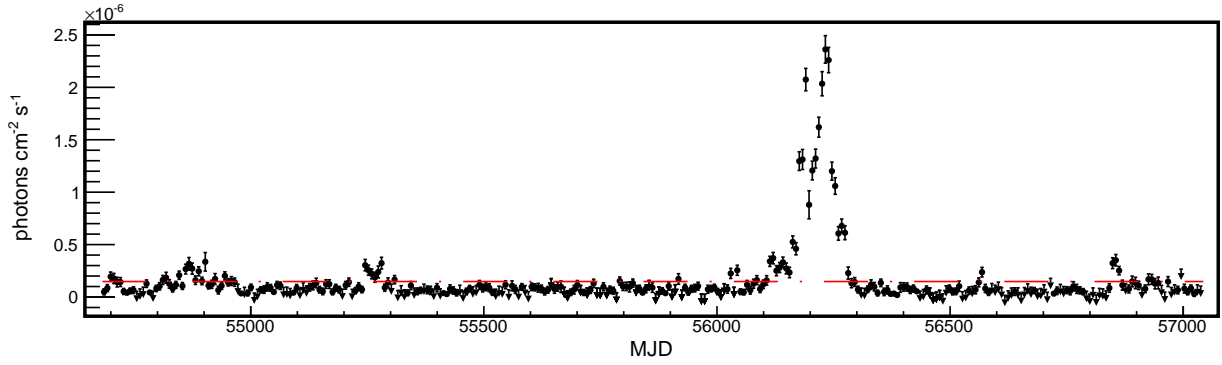


FIG. 4.— *Fermi*-LAT light curve of B2 0218+35 with seven-day binning. The energy range is 100 MeV to 300 GeV.

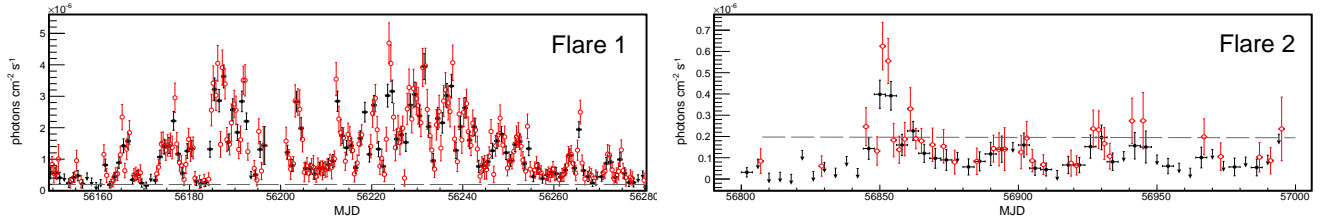


FIG. 5.— *Fermi*-LAT light curves of B2 0218+35 during two flaring periods. The green dashed line represents the average flux ($1.41 \pm 0.04 \times 10^{-7}$ photons cm $^{-2}$ s $^{-1}$) measured from the 6.5 year light curve of B2 0218+35 in the energy range from 100 MeV to 300 GeV. **Top:** Flare 1 with 12-hour binning (black filled circles) and with 6-hour binning (red open circles). **Bottom:** Flare 2 with four-day binning (black filled circles), and two-day binning (red open circles).

domain is the inverse of the relative time delay a . We identify the time delay by calculating and analyzing the power spectrum of the power spectrum that includes the periodic pattern. We apply these methods to the first flaring period in Section 5.1a.

Monte Carlo simulations demonstrate that this signal processing allows removal of the intrinsic variability of the source. We have previously demonstrated that this procedure yields precise and significant estimates of the time delays (Barnacka et al. 2015a).

The DPS method is very efficient when applied to long, evenly sampled light curves. However, sometimes the flare is an isolated event of very short duration like Flare 2. To treat these flares, we use the Maximum Peak Method (MPM, Section 3.2.3, Barnacka et al. 2015a) where we calculate the ratio between the flux in the flare and flux in the subsequent data. We compare the flux ratios as a function of the lag between the brightest flare and the subsequent light curve with the predictions of the model (Section 5.2) of B2 0218+35.

5.1. Flare 1

Enormous gamma-ray activity occurred during the period MJD: 56160 – 56280. We analyze this time interval using the ACF and DPS (see Figure 6). We obtain a time delay of 11.5 ± 0.5 days for the ACF, and 11.38 ± 0.13 days using the DPS.

To estimate the significance of the detection, we use Monte Carlo simulations following Barnacka et al. (2015a). We produce 10^6 artificial light curves.

The temporal behavior of Flare 1 is not power law noise. The flare consists of a superposition of very short duration flares with large amplitudes. Figure 7 compares Flare 1 with the temporal behavior of power law

noise with different indices. The temporal behavior during Flare 1 is not well reproduced by any of these pure noise models. Pink noise ($\alpha \sim 1$) is the closest match. The power spectrum of Flare 1 actually returns $\alpha = 0.9$. However, pink noise is not complete description of temporal behavior of Flare 1 because it cannot account for correlated bin-to-bin time variations of large amplitude. Increasing the index of power law noise (e.g. red noise) smooths the large fluctuations and obviously does not reproduce the behavior of the source. Decreasing the index toward white noise increases the fluctuations on bin-to-bin time scales, but the fast rise exponential decay profile that characterizes flares is absent (Peng et al. 2010; Saito et al. 2013). This correlated behavior resulting from the physics of the source is not reproduced by a simple noise model.

Simulations of the signal composed of superpositions of short and bright flares are possible, but the number of parameters required to define the flares is large. Thus following Barnacka et al. (2011), we divide the light curve into overlapping segments. We can use this approach because the flaring activity lasted for almost 200 days and the range of expected time delays is short, < 20 days. We can thus divide the light curve of Flare 1 into three overlapping segments of 128 days each. We apply the ACF and DPS to each of the three segments and then average the results. The error bars are the standard deviation among the three segments in each bin.

Figure 8 (Left) shows the ACF averaged over the segments. We fit the spectrum with an exponential function representing the background and a Lorentzian function representing the signal. The fit returns a time delay of 11.24 ± 0.39 days. However, the error bars are large and the significance of the signal is only 0.3σ .

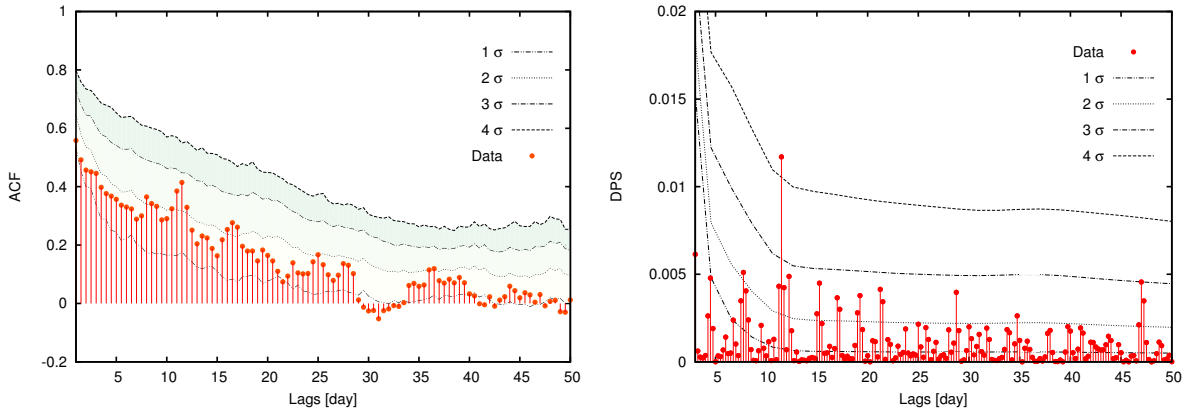
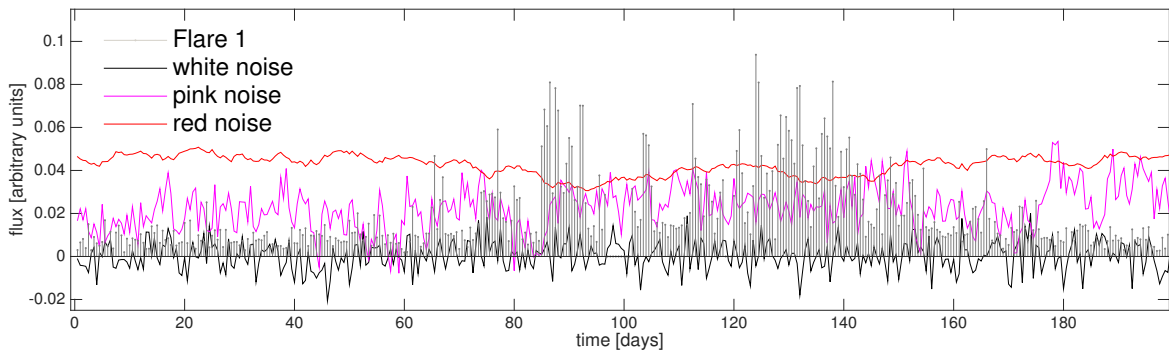
FIG. 6.— Autocorrelation Function (**Left**) and Double Power Spectrum (**Right**) for Flare 1.FIG. 7.— Comparison of the temporal behavior of Flare 1 and power law noise: white noise ($\alpha \sim 0$), pink noise ($\alpha \sim 1$), and red noise ($\alpha \sim 2$). We scale the flux of the Flare 1 by a factor of 2×10^4 to align the data with the simulations. The flux of the pink and red noise are shifted by a factor of 0.02 and 0.04, respectively. The shift in scale avoids overlapping of the plots, and facilitates comparison of the temporal structure.

Figure 8 (Right) shows the DPS from the averaged segments. We fit linear plus Lorentzian profiles to obtain the position of the peak and its significance. The corresponding time delay is 11.33 ± 0.12 days. The signal is 4.13σ above the background. The DPS time delay, detected at high significance, agrees remarkably well with the previously obtained gamma-ray time delay of 11.46 ± 0.16 days reported by [Cheung et al. \(2014\)](#).

The light curve is a superposition of multiple flares. The time between the random flares could mimic a time delay. These “fake” signals should occur only in a fraction of the light curve. A true gravitationally-induced time delay persists over the entire flaring period. The analysis that averages over segments of the light curve distinguishes the real, gravitationally induced, signal from randomly superimposed flares. If there is a real time delay the significance of the time delay increases with averaging over the three periods. For random multiple flares, the significance should not improve. In fact Figure 8 shows that multiple peaks are present because there is a lot of structure in the light curve. However, only the signal in bins around 11.5 days is significant (Figure 8).

5.2. Flare 2

Flare 2, a single, bright flare, occurred in time period MJD: 56800 – 57000. The light curve (2 day bins) around

the flare consists mostly of upper limits (Figure 5). This light curve is useless for extracting several-day long time delays. However, the huge advantage of having a single isolated flare is the ease of a direct search for the echo flare. Figure 9 shows the result of application of the Maximum Peak Method (MPM, Section 3.2.3, [Barnacka et al. 2015a](#)). The MPM method suggests that the time delay lies in one of two ranges: 9.75 ± 0.5 days or 11 ± 0.25 days. The errors corresponds to the bin width, not the 1σ standard deviation.

6. THE STRUCTURE OF THE GAMMA-RAY SOURCE

So far we have used the radio observations and a lens model to reconstruct the origin of the radio core with a resolution of 1 mas (Section 3.2.1). The Fermi-LAT observations enable precise determination of the time delay for two gamma-ray flares (Section 5). Here, we locate the sources of gamma-ray emission relative to the radio core by combining the radio source map and the Fermi-LAT time delays with the well-measured Hubble constant from [Planck Collaboration et al. \(2014\)](#).

[Barnacka et al. \(2015b\)](#) show that the Hubble parameter implied by the time delay is sensitive to any spatial offset between the emission region that produces the resolved mirage images and the site of the variable emission used to measure time delays. Purely on the basis of the physical processes involved, the gamma-ray emis-

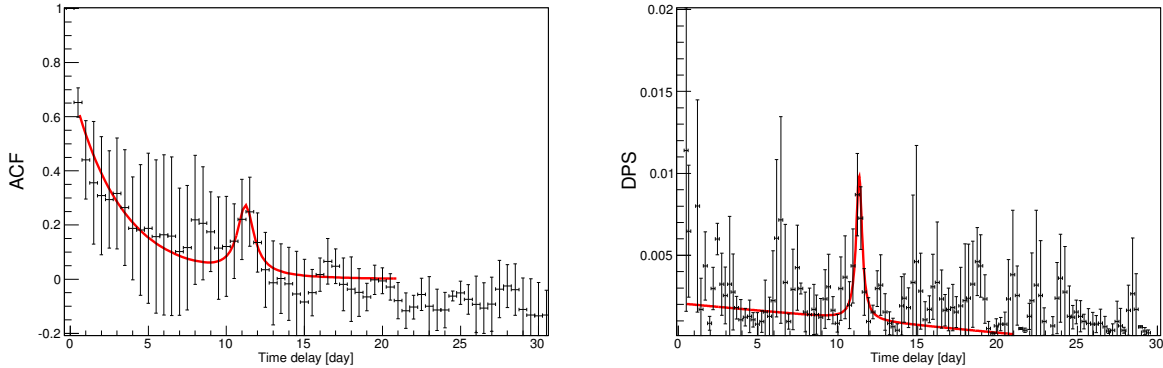


FIG. 8.— Autocorrelation Function (**Left**) and Double Power Spectrum (**Right**) for Flare 1. The spectra are the average of three time sequences.

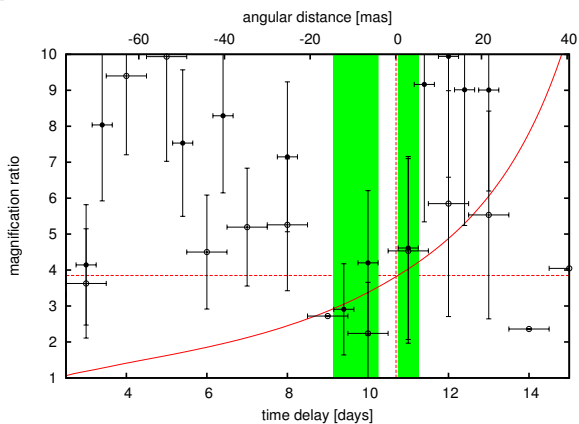


FIG. 9.— The Maximum Peak Method applied to Flare 2. Black and gray points are flux ratios calculated relative to the time bin center at MJD: 56852, using light curve with 0.5 day and 1 day binning, respectively. The solid red line indicates the predicted magnification ratio as a function of the time delay along the jet axis. The red dotted lines indicates the value of the magnification ratio and time delay corresponding to the radio core resolved at 15 GHz. The green area indicates values of time delay where the observed flux ratio is consisted with the model.

sion from B2 0218+35 may not be spatially coincident with the radio core (Barnacka et al. 2014a). The Hubble parameter, well measured with a variety of independent methods, provides a route to exploring this issue. We can use this precisely measured Hubble parameter to evaluate any offset between the radio core and the site of the variable gamma-ray emission. We call this method the Hubble Parameter Tuning (HPT) approach.

The Hubble parameter enters into the distance ratio in the time delay calculation (Eq 2). For an SIS gravitational potential, the relation reduces to:

$$h = \frac{d(1+z_L)(\theta_B^2 - \theta_A^2)}{2c\Delta t}. \quad (6)$$

We have three kinds of constraints on the map of the source from radio to gamma-ray wavelengths: the Hubble parameter, the positions of the lensed images, and the time delay between the images Δt . If there is an offset between the radio core and the gamma-ray emitting regions, the Hubble parameter derived from the Fermi-LAT time delay will differ from the independently measured “true” value. This difference depends on the distance be-

tween the radio core and the spatial location of the flare. The offset in Hubble space corresponds to the spatial offset in the source plane (Barnacka et al. 2015b).

To locate the origin of the gamma-ray flares from B2 0218+35, we first fix θ_A and θ_B to the positions of the resolved images of the 15 GHz radio core (Table 1). We use these image positions along with the model of the lens and the cosmological parameters to infer the expected time delay for the position of the 15 GHz radio core. Table 3 lists the reconstructed position; the value agrees well with the time delay derived from the variability of the radio core although we do not use this delay to compute the Hubble constant. The reconstructed time delay (Table 3) plugged into Equation (6) is a consistency check which returns the true value of the Hubble parameter, our reference point.

Next, we calculate time delays for positions within ~ 10 mas from the radio core. We use these time delays and positions of the 15 GHz images to compute the Hubble parameter using Equation (6). Figure 10 shows these calculated Hubble parameters as a function of the position of the variable emitting region. We call this projection of the model Hubble space.

6.1. The Spatial Origin of Flare 1

Flare 1 has a time delay of 11.33 ± 0.12 days. The Hubble parameter obtained based on the position of the 15 GHz radio core and this time delay corresponds to $H_0 = 63.64 \pm 0.67 \text{ km s}^{-1} \text{ Mpc}^{-1}$. The quoted error corresponds to an error in a time delay of 0.12 days that translates into a spatial resolution of 1.15 mas. Recall that $H_0 = 67.3 \pm 1.2 \text{ km s}^{-1} \text{ Mpc}^{-1}$ from Planck Collaboration et al. (2014).

We indicate the position of the 15 GHz radio core in Hubble space in Figure 10. The Hubble parameter estimated for Flare 1 appears as a red dot in Figure 10. The position of Flare 1 in Hubble space is displaced from the radio core. The resolved radio images also constrain the alignment of the jet as indicated in Figure 10 (white dotted line).

The distance between the 15 GHz core and the site of the gamma-ray flare is 6.4 ± 1.1 mas displaced toward the central engine. This displacement corresponds to a projected distance of 51.2 ± 8.8 pc. The accuracy of the Hubble parameter measured with Planck Collaboration

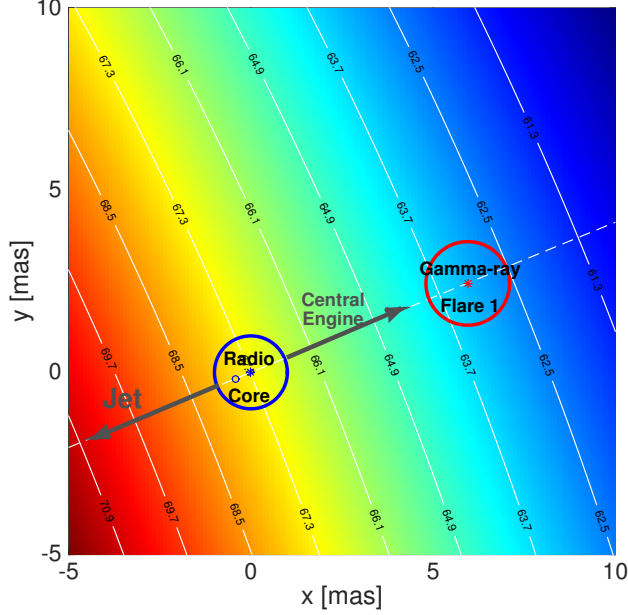


FIG. 10.— Hubble space. The distances are shown with respect to the position of the radio core (blue circle). The radius of the blue circle corresponds to an uncertainty of 1 mas. The blue star indicates the value of the Hubble parameter based on the reconstructed position of the 15 GHz radio core. The open blue point shows the Hubble parameter derived from the observed positions of the 15 GHz radio images. The dotted line shows the jet projection. Gray arrows show the direction from the radio core toward the central engine and toward the jet. The red circle locates the spatial origin of Flare 1. The radius of the red circle corresponds to the uncertainty in the time delay. The spacing of the white lines in Hubble space corresponds to $1.2 \text{ km s}^{-1} \text{ Mpc}^{-1}$, the 1σ uncertainty in the Hubble parameter (Planck Collaboration et al. 2014).

et al. (2014), $\pm 1.2 \text{ km s}^{-1} \text{ Mpc}^{-1}$, implies that the offset between the resolved radio core and the variable gamma-ray site is significant at the $\sim 3\sigma$ level.

6.2. The Spatial Origin of Flare 2

Flare 2 has a time delay in one of two ranges: 10.75 – 11.25 days or 9.25 – 10.25 days. For the first range, the Hubble parameter is $63.64 - 66.6 \text{ km s}^{-1} \text{ Mpc}^{-1}$. The second range results in a Hubble parameter of $69.85 - 77.4 \text{ km s}^{-1} \text{ Mpc}^{-1}$. We indicate the possible sites of Flare 2 in Figure 11. Flare 2 originates either $3.35 \pm 2.30 \text{ mas}$ ($26.8 \pm 18.4 \text{ pc}$ in the source plane) from the core toward the central engine, or $8.33 \pm 4.5 \text{ mas}$ ($66.64 \pm 36.00 \text{ pc}$ in the source plane) in the direction of the jet.

6.3. The Connection between Flare 1 and Flare 2

The Hubble space display shows that Flare 2 is not coincident with either the core or Flare 1. Using the Hubble parameter tuning approach, we can ask whether Flare 2 could result from a moving knot, which first produced Flare 1 and then moved downstream along the jet to produce Flare 2.

The time between the beginning of Flare 1 and Flare 2, Δt_{obs} , is 690 days. The projected distance between Flare 1 and Flare 2, constrained by the time delay of

11 ± 0.25 days, is $D_{\text{projected}} \sim 24 \text{ pc}$. In this case the model implies that knot is moving relativistically with an apparent velocity of β_{app} :

$$\beta_{\text{app}} = \frac{D_{\text{projected}}(1 + z_S)}{c \Delta t_{\text{obs}}} \approx 70 \left(\frac{D_{\text{projected}}}{24 \text{ pc}} \right) \left(\frac{\Delta t_{\text{obs}}}{690 \text{ days}} \right). \quad (7)$$

Similar superluminal apparent motions of $\sim 46c$ occur, for example, in the radio jet of PKS 1510-089 (Jorstad et al. 2005). This time delay thus yields a reasonable physical model for the gamma-ray source.

If the plasmon continues its motion with the same apparent velocity, 1.6 mas/year , it will pass through the stationary shock of the 15 GHz core $\sim 2 \pm 1$ years after Flare 2, which was detected in July 2014. This model thus predicts increased radio emission in the time period around July 2016. Radio observations during this period could thus provide valuable insight into the physical processes and plasma propagation along the jet.

The second possible site of Flare 2, implied by the time delay of $\sim 9.75 \pm 0.5$, is located at a projected distance of $\sim 16 \text{ mas}$ from Flare 1. An apparent velocity of $350c$ would be required to explain such a large projected distance. Thus, these flares could not be produced by the same moving knot of plasma.

We do not have direct evidence that Flare 2 is indeed connected with Flare 1. However, the longer time delay implies a reasonable physical model for the source and demonstrates the power of the Hubble parameter tuning approach.

7. DISCUSSION

A major challenge of gamma-ray astronomy is localization of the emission region. The blazar B2 0218+35 is uniquely suited to detailed reconstruction of the source position. The gravitational lensing system is remarkably simple. There are exquisite radio data at several wavelengths along with the extensive Fermi-LAT light curve. These observations combined with the well-constrained Hubble constant enable the first reconstruction of the gamma-ray source positions relative to the radio core and jet.

Application of the method to other sources may not be as straightforward. For example, the mass distribution of the lens might be more complex thus limiting the spatial resolution of the lens. The radio data might be insufficient to reconstruct the projection of the jet. Furthermore, observations of relatively nearby sources show that jets can be bent, thus introducing additional uncertainty in measuring distances between emitting regions.

7.1. Comparison with PKS1830-211

PKS 1830-211 is the only other gravitationally lensed gamma-ray blazar known currently. Analysis of the gamma-ray time delays enable resolution of the origin of gamma-ray flares at the $\sim 10 \text{ mas}$ level, corresponding to $\sim 100 \text{ pc}$ in the source plane (Barnacka et al. 2015a). In this case, the spatial resolution is limited by the accuracy of time delay, ~ 0.5 days.

Flare 1 of B2 0218+35 was longer and brighter than the flares of PKS 1830-211. The excellent photon statistics of Flare 1 allow measurement of the time delay with an

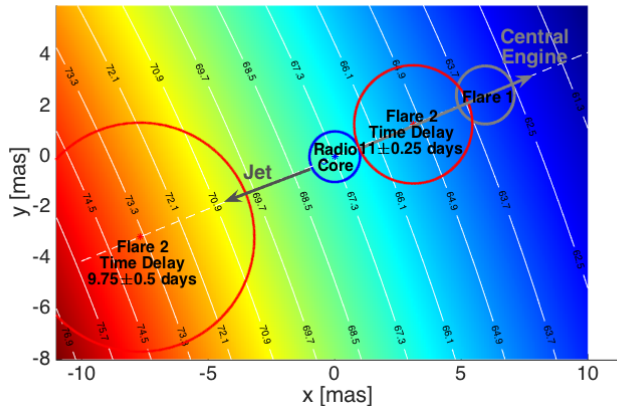


FIG. 11.— Hubble space calculated as in Figure 10. Red circles show the two possible sites for the spatial origin of Flare 2 corresponding to a time delay of 9.75 ± 0.5 days or 11 ± 0.25 days. accuracy of ~ 0.1 days, an improvement by a factor of 5 relative to PKS 1830-211.

In PKS 1830-211 there is no Einstein ring. The pseudo-ring-like structure composed of images of the radio jet only allow derivation of a boundary limiting the jet projection in the source plane.

In contrast with PKS 1830-211, the well-resolved radio images and the more accurate gamma-ray time delay enable relative localization of the radio and gamma-ray sources if the Hubble constant is sufficiently well-known from some independent technique. We can separate Flare 1 from the core in B2 0218+35 at the $\sim 3\sigma$ level because the Hubble parameter is measured with $\sim 2\%$ accuracy using the cosmic microwave background fluctuations (Planck Collaboration et al. 2014).

Future measurement of the Hubble parameter with an accuracy of $\sim 1\%$ (Bennett et al. 2014) will allow resolution of the gamma-ray emission at even greater significance, $\sim 6\sigma$.

7.2. The Spatial Origin of Gamma-ray Flares and Source Physics

The spatial origin of gamma-ray flares is a subject of debate (Nalewajko et al. 2014a; Tavecchio et al. 2010). Some observations indicate that flares are produced upstream from the resolved radio core (Marscher et al. 2008, 2010; Karamanavis et al. 2015). However, most theoretical models assume that dissipation takes place within a sub-parsec scale from the central engine, where the plasma is denser and the sources of seed photons for inverse-Compton radiation are abundant (Nalewajko et al. 2014b; Barnacka et al. 2014b; Hovatta et al. 2015; Tanaka et al. 2011).

Only radio telescopes can resolve scales smaller than 100 pc. Radio telescopes probe synchrotron radiation produced in optically thick parts of the jet. The radio core is often interpreted as the location where the jet opacity to synchrotron self-absorption is 1 (Blandford & Königl 1979). Observationally, the radio core is the region of peak intensity generated by a compact component at the apparently upstream end of the jet (Marscher 2008; Haga et al. 2015).

Measurement of the distance between a radio core and the central engine is difficult. These measurements have

only been possible for nearby sources with prominent two-sided jets. Observing outflows in two opposite directions then constrains the position of the central engine (Haga et al. 2015).

For gamma-ray blazars the two-sided jet is presumably present, but the counterjet is too faint for detection because of relativistic beaming. Thus, in blazars, we observe only one sided-jets. As summarized by Haga et al. (2015), the general picture is that a central engine exists somewhere upstream of observed cores. B2 0218+35 provides the first direct observational constraint.

In B2 0218+35 the bright gamma-ray flare occurred upstream in the jet at the projected distance of 51.2 ± 8.8 pc from the 15 GHz radio core. Thus the central engine must be at least this far away from the radio core. The Hubble tuning approach we use can enable measurement of the apparent velocities of gamma-ray emitting knots. Based on this measurement, we can predict the time of a plausible interaction with the radio core. For B2 0218+35 we predict increased emission at gamma ray and/or radio wavelengths within a year of July 2016.

7.3. Gravitational Lensing and X-ray Sources

The improvement of angular resolution at X-ray wavelengths with *Chandra* enabled the discovery of high energy extragalactic jets extending over hundreds of kiloparsecs (Harris & Krawczynski 2006; Tavecchio et al. 2007; Siemiginowska et al. 2002; Biretta et al. 1991). In fact, our investigations of the structure of lensed gamma-ray sources were inspired by *Chandra*'s discovery of flaring emission from HST-1, a knot of strong X-ray emission displaced from the core in the nearby galaxy M87 (Harris et al. 2006). Recently, deep *Chandra* observations of Pictor A revealed the high-energy flares located in knots displaced along the jet (Hardcastle et al. 2015).

For sources at redshift ~ 1 , the *Chandra* resolution of 0.5 arcseconds corresponds to 4 kpc. Thus, knots like HST-1 cannot be resolved. Improvement in angular resolution of at least two orders of magnitude is needed to resolve these sources and to explore their evolution.

There are, however, ~ 20 gravitationally lensed quasars with associated X-ray emission. The sources have been monitored in searches for microlensing (Chartas et al. 2002; Dai et al. 2003; Chartas et al. 2012; Chen et al. 2012; Mosquera et al. 2013). These data and future monitoring of variable X-ray sources may enable measurement of time delays.

These sources have been also monitored at radio and optical wavelengths. Combining these observations along the lines we have followed for B2 0218+35 may enable reconstruction of these sources based on lensing models. If displacements of the X-ray emitting regions along the jets are common, they pose challenges to understanding of the particle acceleration mechanism. They may also increase our understanding of the distribution of Hubble constants derived from time delays (Barnacka et al. 2015b).

7.4. Gravitational Lensing and SKA

SKA will observe thousands of gravitationally lensed quasars with a resolution of ~ 2 mas at 10 GHz, and ~ 20 mas at 1 GHz (Dewdney et al. 2009; Godfrey et al. 2012; McKean et al. 2015). These radio observations will

provide a foundation for reconstructing the mass distribution of lenses and the positions of radio cores.

All radio quasars have X-ray emission (Risaliti & Lusso 2015). Thus, among these lensed systems, there will be a large population of quasars with variable high energy emission where time delays can be measured.

An ensemble of high-energy quasars with measured time delays and reconstructed source structure based on robust lensing models will enable investigation of the origin of X-ray radiation and the connection between the radio and high-energy emission. The large redshift range of lensed quasars should provide constraints on the co-evolution of radio and high-energy jets.

8. CONCLUSIONS

B2 0218+35 is one of only two known gravitationally lensed systems detected at gamma rays. We reconstruct the mass distribution of its lensing galaxy and the properties of the jet based on well-resolved radio observations. We use the dense Fermi-LAT light curves to measure time delays for two gamma-ray flares. The position of the mirage images, the time delay, and the independently known Hubble constant enable measurement of the spatial offset between the gamma-ray emission region and the radio core.

Our reconstruction of the lensed source shows that the extended flare (Flare 1) is displaced from the radio core at the $\sim 3\sigma$ level. The displacement is upstream from the jet providing the first direct observational constraint on the location of the central engine relative to the radio core for blazars.

A shorter flare (Flare 2) may be an event following

Flare 1. If Flare 1 and Flare 2 are indeed connected then the knot which produced these gamma-ray flares moves at apparent velocity of $\sim 70c$. Thus the model makes a testable prediction. There should be an interaction with the radio core within a year of July 2016.

The only other known gravitationally lensed gamma-ray blazar is PKS 1830-211. This source also has complex structure with gamma-ray flares originating from multiple regions along the jet (Barnacka et al. 2011, 2015a).

Lensed high-energy sources monitored with detectors like *Chandra*, Swift and NuSTAR offer rich opportunities to extend this powerful lens modeling approach to other sources. There are more than 20 known lensed quasars with associated X-ray emission. Some of these systems already have enough observations to reconstruct the mass distribution of the lens. Further monitoring will enable measurement of time delays with X-ray detectors.

In the near future, SKA will resolve thousands of radio images of gravitationally lensed quasars. Many of these quasars will also have prominent variable X-ray emission, allowing recovery of time delays. This ensemble of observations combined with the power of strong gravitational lensing will probe the origin of X-ray radiation, its connection to radio emission, and the cosmic evolution of jets at radio and high energies.

We thank Scott Kenyon for valuable comments.

A.B. is supported by NASA through Einstein Postdoctoral Fellowship. MJG is supported by the Smithsonian Institution.

REFERENCES

- Atwood, W. B., Abdo, A. A., Ackermann, M., et al. 2009, *ApJ*, 697, 1071
- Barnacka, A. 2013, ArXiv e-prints, arXiv:1307.4050
- Barnacka, A., Geller, M. J., Dell’Antonio, I. P., & Benbow, W. 2014a, *ApJ*, 788, 139
- . 2015a, *ApJ*, 809, 100
- . 2015b, *ApJ*, 799, 48
- Barnacka, A., Glicenstein, J.-F., & Moudden, Y. 2011, *A&A*, 528, L3
- Barnacka, A., Moderski, R., Behera, B., Brun, P., & Wagner, S. 2014b, *A&A*, 567, A113
- Bennett, C. L., Larson, D., Weiland, J. L., & Hinshaw, G. 2014, *ApJ*, 794, 135
- Biggs, A. D., Browne, I. W. A., Helbig, P., et al. 1999, *MNRAS*, 304, 349
- Biggs, A. D., Browne, I. W. A., Jackson, N. J., et al. 2004, *MNRAS*, 350, 949
- Biggs, A. D., Browne, I. W. A., Muxlow, T. W. B., & Wilkinson, P. N. 2001, *MNRAS*, 322, 821
- Biggs, A. D., Wucknitz, O., Porcas, R. W., et al. 2003, *MNRAS*, 338, 599
- Biretta, J. A., Stern, C. P., & Harris, D. E. 1991, *AJ*, 101, 1632
- Blandford, R., & Narayan, R. 1986, *ApJ*, 310, 568
- Blandford, R. D., & Königl, A. 1979, *ApJ*, 232, 34
- Bogert, B. P., Healy, M. J. R., & Tukey, J. W. 1963, in *Proceedings on the Symposium on Time Series Analysis*, ed. M. Rosenblatt, Wiley, NY, 209–243
- Broderick, A. E., & Tchekhovskoy, A. 2015, *ApJ*, 809, 97
- Browne, I. W. A., Patnaik, A. R., Walsh, D., & Wilkinson, P. N. 1993, *MNRAS*, 263, L32
- Cerutti, B., Werner, G. R., Uzdensky, D. A., & Begelman, M. C. 2012, *ApJ*, 754, L33
- Chartas, G., Agol, E., Eracleous, M., et al. 2002, *ApJ*, 568, 509
- Chartas, G., Kochanek, C. S., Dai, X., et al. 2012, *ApJ*, 757, 137
- Chávez, R., Terlevich, E., Terlevich, R., et al. 2012, *MNRAS*, 425, L56
- Chen, B., Dai, X., Kochanek, C. S., et al. 2012, *ApJ*, 755, 24
- Cheung, C. C., Larsson, S., Scargle, J. D., et al. 2014, *ApJ*, 782, L14
- Cohen, A. S., Hewitt, J. N., Moore, C. B., & Haarsma, D. B. 2000, *ApJ*, 545, 578
- Cohen, J. G., Lawrence, C. R., & Blandford, R. D. 2003, *ApJ*, 583, 67
- Corbett, E. A., Browne, I. W. A., Wilkinson, P. N., & Patnaik, A. 1996, in *IAU Symposium, Vol. 173, Astrophysical Applications of Gravitational Lensing*, ed. C. S. Kochanek & J. N. Hewitt, 37
- Dai, X., Chartas, G., Agol, E., Bautz, M. W., & Garmire, G. P. 2003, *ApJ*, 589, 100
- Dewdney, P. E., Hall, P. J., Schilizzi, R. T., & Lazio, T. J. L. W. 2009, *IEEE Proceedings*, 97, 1482
- Efstathiou, G. 2014, *MNRAS*, 440, 1138
- Freedman, W. L., & Madore, B. F. 2010, *ARA&A*, 48, 673
- Freedman, W. L., Madore, B. F., Scowcroft, V., et al. 2012, *ApJ*, 758, 24
- Freedman, W. L., Madore, B. F., Gibson, B. K., et al. 2001, *ApJ*, 553, 47
- Giannios, D., Uzdensky, D. A., & Begelman, M. C. 2009, *MNRAS*, 395, L29
- Godfrey, L. E. H., Bignall, H., Tingay, S., et al. 2012, *Publications of the Astronomical Society of Australia*, 29, 42
- Haario, H., Laine, M., Mira, A., & Saksman, E. 2006, *Statistics and Computing*, 16, 339
- Haga, T., Doi, A., Murata, Y., et al. 2015, *ApJ*, 807, 15
- Hardcastle, M. J., Lenc, E., Birkinshaw, M., et al. 2015, ArXiv e-prints, arXiv:1510.08392
- Harris, D. E., Cheung, C. C., Biretta, J. A., et al. 2006, *ApJ*, 640, 211
- Harris, D. E., & Krawczynski, H. 2006, *ARA&A*, 44, 463
- Hoshino, M. 2012, *Physical Review Letters*, 108, 135003

- Hovatta, T., Petropoulou, M., Richards, J. L., et al. 2015, *MNRAS*, 448, 3121
- Jackson, N., Xanthopoulos, E., & Browne, I. W. A. 2000, *MNRAS*, 311, 389
- Jaroschek, C. H., Treumann, R. A., Lesch, H., & Scholer, M. 2004, *Physics of Plasmas*, 11, 1151
- Jorstad, S. G., Marscher, A. P., Lister, M. L., et al. 2005, *AJ*, 130, 1418
- Karamanavis, V., Fuhrmann, L., Krichbaum, T. P., et al. 2015, *ArXiv e-prints*, arXiv:1511.01085
- Kirk, J. G., & Skjæraasen, O. 2003, *ApJ*, 591, 366
- Kneib, J. P. 2014, *Manual of the LensTool program*
- Kochanek, C. S., & Dalal, N. 2004, *ApJ*, 610, 69
- Komissarov, S. S., Barkov, M. V., Vlahakis, N., & Königl, A. 2007, *MNRAS*, 380, 51
- Larchenkova, T. I., Lutovinov, A. A., & Lyskova, N. S. 2011, *Astronomy Letters*, 37, 233
- Lehár, J., Falco, E. E., Kochanek, C. S., et al. 2000, *ApJ*, 536, 584
- Lyubarsky, Y. E. 2005, *MNRAS*, 358, 113
- Lyutikov, M., & Uzdensky, D. 2003, *ApJ*, 589, 893
- MacDonald, N. R., Marscher, A. P., Jorstad, S. G., & Joshi, M. 2015, *ApJ*, 804, 111
- Mao, S., & Schneider, P. 1998, *MNRAS*, 295, 587
- Marscher, A. P. 2008, in *Astronomical Society of the Pacific Conference Series*, Vol. 386, *Extragalactic Jets: Theory and Observation from Radio to Gamma Ray*, ed. T. A. Rector & D. S. De Young, 437
- Marscher, A. P., Jorstad, S. G., D’Arcangelo, F. D., et al. 2008, *Nature*, 452, 966
- Marscher, A. P., Jorstad, S. G., Larionov, V. M., et al. 2010, *ApJ*, 710, L126
- Mattox, J. R., Bertsch, D. L., Chiang, J., et al. 1996, *ApJ*, 461, 396
- McKean, J., Jackson, N., Vegetti, S., et al. 2015, *Advancing Astrophysics with the Square Kilometre Array (AASKA14)*, 84
- McKinney, J. C. 2006, *MNRAS*, 368, 1561
- Metcalf, R. B., & Amara, A. 2012, *MNRAS*, 419, 3414
- Mittal, R., Porcas, R., & Wucknitz, O. 2007, *A&A*, 465, 405
- Moscibrodzka, M., Falcke, H., & Shiokawa, H. 2015, *ArXiv e-prints*, arXiv:1510.07243
- Mosquera, A. M., Kochanek, C. S., Chen, B., et al. 2013, *ApJ*, 769, 53
- Nalewajko, K., Begelman, M. C., & Sikora, M. 2014a, *ApJ*, 789, 161
- Nalewajko, K., Giannios, D., Begelman, M. C., Uzdensky, D. A., & Sikora, M. 2011, *MNRAS*, 413, 333
- Nalewajko, K., Sikora, M., & Begelman, M. C. 2014b, *ApJ*, 796, L5
- Nalewajko, K., Uzdensky, D. A., Cerutti, B., Werner, G. R., & Begelman, M. C. 2015, *ArXiv e-prints*, arXiv:1508.02392
- Narayan, R., & Bartelmann, M. 1996, *ArXiv Astrophysics e-prints*, astro-ph/9606001
- Nolan, P. L., Abdo, A. A., Ackermann, M., et al. 2012, *ApJS*, 199, 31
- O’Dea, C. P., Baum, S. A., Stanghellini, C., et al. 1992, *AJ*, 104, 1320
- Patnaik, A. R., Browne, I. W. A., King, L. J., et al. 1993, *MNRAS*, 261, 435
- Patnaik, A. R., Browne, I. W. A., Wilkinson, P. N., & Wrobel, J. M. 1992, *MNRAS*, 254, 655
- Patnaik, A. R., Porcas, R. W., & Browne, I. W. A. 1995, *MNRAS*, 274, L5
- Peng, Z. Y., Yin, Y., Bi, X. W., et al. 2010, *ApJ*, 718, 894
- Planck Collaboration, Ade, P. A. R., Aghanim, N., et al. 2014, *A&A*, 571, A16
- Proga, D. 2005, *ApJ*, 629, 397
- Riess, A. G., Macri, L., Casertano, S., et al. 2011a, *ApJ*, 730, 119
- . 2011b, *ApJ*, 732, 129
- Risaliti, G., & Lusso, E. 2015, in *Exploring the Hot and Energetic Universe*, ed. M. Ehle, 26
- Saito, S., Stawarz, L., Tanaka, Y. T., et al. 2013, *ApJ*, 766, L11
- Siemiginowska, A., Bechtold, J., Aldcroft, T. L., et al. 2002, *ApJ*, 570, 543
- Sironi, L., & Spitkovsky, A. 2014, *ApJ*, 783, L21
- Stawarz, L., & Ostrowski, M. 2002, *ApJ*, 578, 763
- Suyu, S. H., Marshall, P. J., Auger, M. W., et al. 2010, *ApJ*, 711, 201
- Suyu, S. H., Auger, M. W., Hilbert, S., et al. 2013, *ApJ*, 766, 70
- Tanaka, Y. T., Stawarz, L., Thompson, D. J., et al. 2011, *ApJ*, 733, 19
- Tavecchio, F., Ghisellini, G., Bonnoli, G., & Ghirlanda, G. 2010, *MNRAS*, 405, L94
- Tavecchio, F., Maraschi, L., Wolter, A., et al. 2007, *ApJ*, 662, 900
- Tchekhovskoy, A., Narayan, R., & McKinney, J. C. 2010, *ApJ*, 711, 50
- . 2011, *MNRAS*, 418, L79
- Vovk, I., & Neronov, A. 2015, *ArXiv e-prints*, arXiv:1507.01092
- Wucknitz, O., Biggs, A. D., & Browne, I. W. A. 2004, *MNRAS*, 349, 14
- York, T., Jackson, N., Browne, I. W. A., Wucknitz, O., & Skelton, J. E. 2005, *MNRAS*, 357, 124
- Zenitani, S., & Hoshino, M. 2001, *ApJ*, 562, L63
- . 2007, *ApJ*, 670, 702
- Zitrin, A., Broadhurst, T., Umetsu, K., et al. 2009, *MNRAS*, 396, 1985
- Zitrin, A., Meneghetti, M., Umetsu, K., et al. 2013, *ApJ*, 762, L30
- Zweibel, E. G., & Yamada, M. 2009, *ARA&A*, 47, 291